

Full Paper

Journal of Space Exploration

WWW.MEHTAPRESS.COM

Giuseppe Pezzella

Centro Italiano Ricerche Aerospaziali,
via Maiorise, 81043 Capua, (ITALY)
E-mail: g.pezzella@cira.it

Received: January 11, 2013

Accepted: February 28, 2013

Published: March 30, 2013

*Corresponding author's Name & Add.

Giuseppe Pezzella
Centro Italiano Ricerche Aerospaziali, via
Maiorise, 81043 Capua, (ITALY)
E-mail: g.pezzella@cira.it

Ablative heat shield design for a sample return vehicle

Abstract

This paper provides a partial overview of the analysis approach typically followed within sample return vehicle design. A more systematic survey was out of the scope of the paper, but it gives some indications concerning main design topics to address in designing such a kind of vehicle for planetary exploration, as for example, effects of heat shield ablation and flow plasma radiation coupling with computational flowfield analysis.

Keywords

Sample return mission; Computational fluid dynamics; Heat shield ablation; Hypersonic flow; Aerothermodynamics.

INTRODUCTION

Sample return mission aims for returning extraterrestrial material sampled in the outer space (e.g., beyond the Moon), for example from comet or planets as Mars to Earth. Such a kind of mission is very important because of an important step forward for Space Exploration activities and for a more accurate knowledge of the Earth and Universe is to select, collect and finally return extraterrestrial samples to Earth where to perform their analysis.

In this framework this paper performs an overview on design method approach which can be used to address the design of a generic sample return capsule (SRC). Generally speaking, the design process demands of satisfying some set of requirements, usually in some optimal manner.

To attain this optimal solution, or at least to satisfy as many as all possible of the imposed requirements, usually it requires tradeoffs between individual elements or systems. To mediate these tradeoffs requires an engineering familiarity and literacy, if not outright talent, with all of the systems and engineering disciplines involved. Spacecraft represent particularly broad challenges, in that a wide range of disciplines is involved – communications, power, thermal control, propulsion and so on.

Arguably, planetary probes are even broader, in that all the usual spacecraft disciplines are involved, plus several aspects related to delivery to and operation in planetary environments, such as aerothermodynamics, soil mechanics and so on. It is crucial that the requirements be articulated in a manner that adequately captures the intent of the “customer”.

Anyway, once mission requirements and constraints are established, the SRC design analysis starts taking into account for design results, available both from literature and previous missions, throughout similarity and scaling processes.

GUIDELINE FOR SAMPLE RETURN VEHICLES DESIGN

The analytical, computational and experimental methods described in this chapter can be used to address the design of a generic sample return vehicle (SRV).

Generally speaking, the design process demands different stages which may require several iterations to obtain an optimization of SRV design. For instance, a typical scheme that synthesizes the design process of a SRV is shown in Figure 1.

Once mission requirements and constraints are established, the SRV design analysis starts taking into account for de-

sign results, available both from literature and previous missions, throughout similarity and scaling processes. This phase is most important considering that it represents the initial condition from which the SRV design evolves and matures. For example, the design starts basing on initial assumptions as SRV configuration, mass, stability considerations during entry, descent and landing environment. Hence, the ballistic parameter is estimated from size, weight and drag coefficient early evaluated. This value of ballistic coefficient is then used to calculate atmospheric trajectories and perform parametric analysis of SRV re-entry flight, and so on.

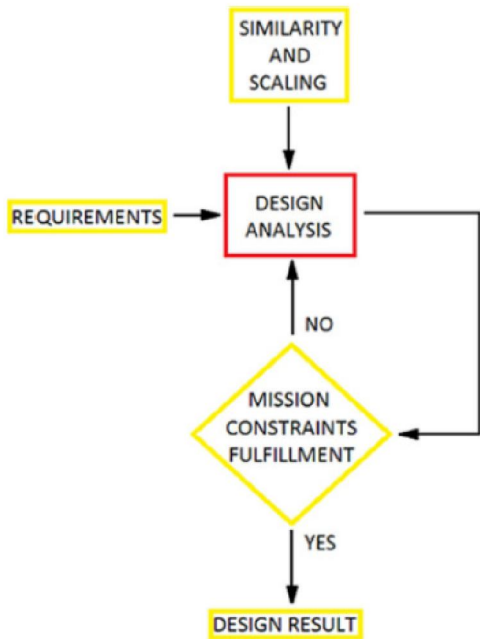


Figure 1 : Typical design process scheme.

Requirements and constraints

In the framework of the design of any space mission both requirements and constraints must be considered. Example of constraints for SRV are the curve limits of the re-entry corridor such as re-entry velocity fixed to about 12 km/s for an altitude of 200 Km, maximal deceleration below 100 g, maximum heat flux below 15 MW/m² and total heat load below 300-350 MJ/m²[1]. Hence, once the heat flux has been estimated, one can calculate the stagnation pressure, thus evaluating approximate TPS layout and thickness. Typical requirements limits are: Landing, Maximal carrying capacity with minimal total volume, Stability during entry, descent and landing, Maximal heat flux, Maximum heat load, Maximum g-load, Impact velocity and Maximum TPS ratio.

On the other hand, typical constraints are: initial entry velocity into Earth is (given by a mission analysis and it is equal to) 12.3 km/s for an altitude of 120 km; the landing on Earth shall be performed with a fully passive entry (no

parachute) for the SRV. The latter constraint represents one of the main considerations in entry vehicle design: i.e. if a parachute system should be included. The advantages of parachute recovery are: entry vehicle tracking at high altitude is easier; the probe or canister has a lower ground impact velocity; recovery operations are easier (the probe is easier to find). Disadvantages may include: slight increase in mass; increased mechanical complexity with the separation of the probe from the aft-cover and parachute; slight decrease in static stability margin.

A small parachute may be able to decelerate the entry vehicle adequately. Even though impact-area drift may increase significantly, ground radar should be able to track the probe and parachute to ensure efficient recovery operations. In this case, the landing on Earth shall be performed with a fully passive ballistic entry (no parachute).

Similarity and scaling

Generally speaking, a preliminary design of any space mission is obtained comparing the requirements of this mission with the requirements of previous ones. Therefore, it is useful to find missions which have similar characteristics to our and use them to obtain a work line. Obviously, some data (capsule size, re-entry velocity, etc..) will be different to ours, so we can adapt these to our mission through a scaling process. In the TABLE 1 some examples of the entry capsules which can be taken as a guideline are summarized^[1,2].

TABLE 1 : Overview of some fundamental SRV parameters^[2].

	Stardust	Genesis	Hayabusa	Marco Polo
R_{nose} m/cone angle °	0.23/60	0.43/60	0.202/45	0.41/45
V_{entry} km/s	12.6	11	11.3	11.8
γ_{entry} °	-8.2	-8	-13.8	-12
M kg	45.8	210	16.3	76
Ballistic coef kg/m ²	60	80	113.5	70
Area m ²	0.56	1.78	0.128	0.95
\dot{Q}_{max} MW/m ²	13	7	15	11
$\int_0^{t^{(end)}} \dot{Q} dt$ MJ/m ²	360	166	320	210
TPS material / mass frac.	PICA-15/ 22%	C-C/ 18%	C phenol/ 43%	PICA?/ 38%

Example of SRC configurations are summarized in Figure 2 to Figure 4.

Figure 2 shows an overview of both internal and external layout of Stardust and Genesis sample return capsules^[2]. An overview of main mission parameters such as trajectory, vehicle geometry, aerothermal environment, and TPS for both Stardust and Genesis SRV can be recognized in TABLE 2 and TABLE 3, respectively^[3]. It is worth to note that the SRV layout is an extremely important design issue. For instance, it determines the position of the vehicle centre-of-mass (CoM). In fact, if a non-spherical

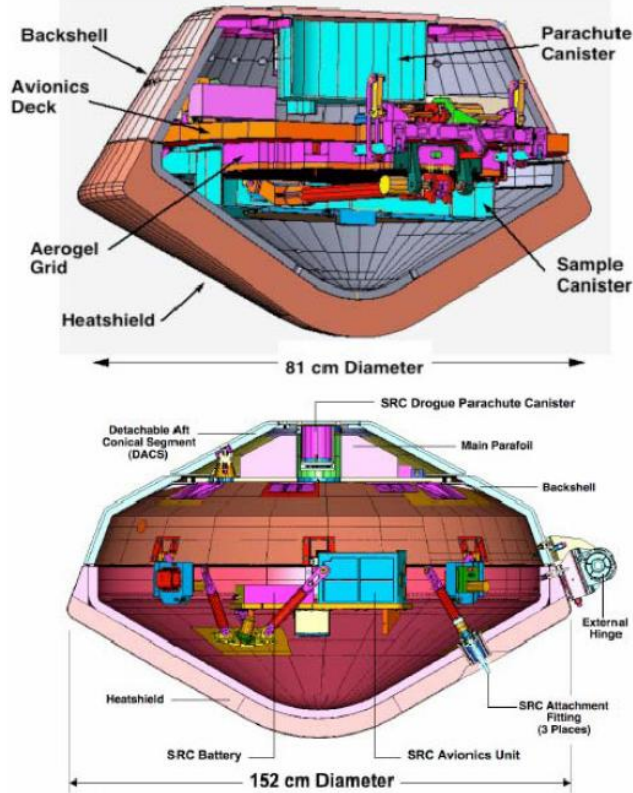


Figure 2 : Stardust (up) and genesis (down) sample return capsules^[2].

entry shell is used, the centre-of-mass of the configuration must lie adequately below the aeroshell's centre-of-pressure (CoP), which in turn moves the spacecraft and its dense components (batteries, etc.) closer to the leading face of the entry shell. If the offset between the CoM and CoP is made too small, then the craft may be unstable to disturbances and make large pitching movements, exposing non-shielded parts to the energetic airflow. As an example, a craft's transition from supersonic to subsonic speed causes changes in the wake flow which in turn can be coupled to the craft, destabilizing it. Some entry spacecraft, such as that of the Genesis sample-return mission, are designed to deploy small drogue parachutes at supersonic speeds to provide extra stability through the transonic region^[4].

Figure 3 to Figure 7 highlight examples of SRV design study results.

Figure 3 shows a typical SRV configuration under investigation in Europe so far^[2]. Such a configuration relies on a sphero-conical aeroshell with a 45 deg half cone angle, a 1.1 m diameter front shield and a smaller back-cover.

In Figure 4 is reported the configuration of the Hayabusa SRC, whose main mission parameters are summarized in TABLE 4^[3].

TABLE 2 : Overview of the Stardust main parameters^[3].

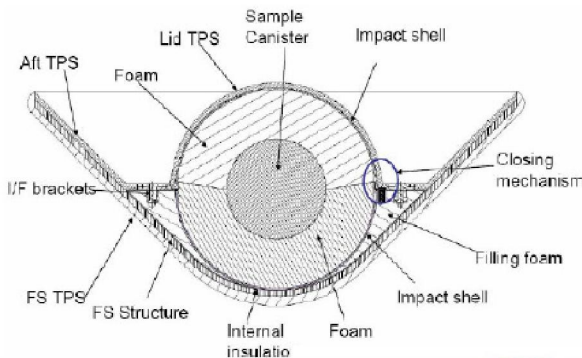
Trajectory		Geometry		Aero/thermal		TPS	
Entry angle	-8.2° ± 0.08° @ 125 km	Shape	Blunt-nosed 60° half-angle cone	Trim L/D (specify trim α)	0	Material designation	PICA-15
Inertial entry velocity	12.8 km/s @ 125 km	Nose radius	0.23 m initial	Ballistic coeff (Ablated).	60.0 kg/m ² 60.4 kg/m ²	Thickness	5.82 cm
Relative entry velocity	12.6 km/s @ 125 km	Base area (Ablated)	0.52 m ² 0.50 m ²	Stagnation heating rate	(non-ablating) 1200 W/cm ²	Ablating? Ejected?	Yes No
Velocity at peak heat	11.1 km/s	Vehicle mass	45.8 kg	Integrated heat load	36,000 J/cm ²	Resin mat. Matrix mat.	Phenolic Carbon fiber
Control method	Ballistic	TPS mass fraction, inc. insul.	22%	Radiative heat flux	130 W/cm ²	Resin dens. Matrix density	109 kg/m ³ 160 kg/m ³
Center of Gravity, X _{CG} /D	.35	Payload mass		PH stag. pressure	0.275 atm	Total material density	250 kg/m ³ approx.

As far as Flight Mechanics is concerned, Figure 5 shows a typical re-entry corridor of a SRV reported in the flight path angle (FPA) ballistic coefficient map. Of course, the green-surface represents the flyable conditions during

descent. This re-entry envelope refers to an atmospheric velocity of 11.8 km/s, at -12 deg FPA, landing load on the sample of 800 g, peak heat flux of 11.3 MW/m², heat load of 209 MJ/m², and entry duration of 484 s^[1,2].

TABLE 3 : Overview of the Genesis main parameters^[3].

<i>Entry angle</i>	-8°	<i>Shape</i>	59.81° blunt cone	<i>Trim L/D (specify trim α)</i>	0	<i>Material designation</i>	Fore: Carbon-carbon Aft: SLA-561V
<i>Inertial entry velocity</i>	11.0 km/s	<i>Nose radius</i>	.43 m	<i>Ballistic coeff.</i>	80 kg/m ³	<i>Thickness</i>	6 cm
<i>Relative entry velocity</i>	10.8 km/s	<i>Base area</i>	1.78 m ²	<i>Stagnation heating rate</i>	700 W/cm ²	<i>Ablating? Ejected?</i>	Partially No
<i>Velocity at peak heat</i>	9.2 km/s	<i>Vehicle mass</i>	210 kg	<i>Integrated heat load</i>	16,600 J/cm ²	<i>Resin mat. Matrix mat.</i>	
<i>Control method</i>	Spin-stabilized aero-ballistic	<i>TPS mass fraction, inc. insul.</i>	~18%	<i>Radiative heat flux</i>	30 W/cm ²	<i>Resin dens. Matrix density</i>	
<i>Center of Gravity, X_{CG}/D</i>	.33	<i>Payload mass</i>		<i>PH stag. pressure</i>		<i>Total material density</i>	



- Mass € [40-80] kg
- 45° half-cone angle
- 1 m diameter
- Norcoat-Liege for back cover
- Landing velocity € [30-40] m.s⁻¹
- 100 mm of ~ 200 kg.m⁻³ PU foam (TBC)

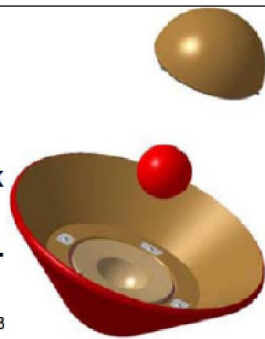


Figure 3 : Example of SRV study results^[2].

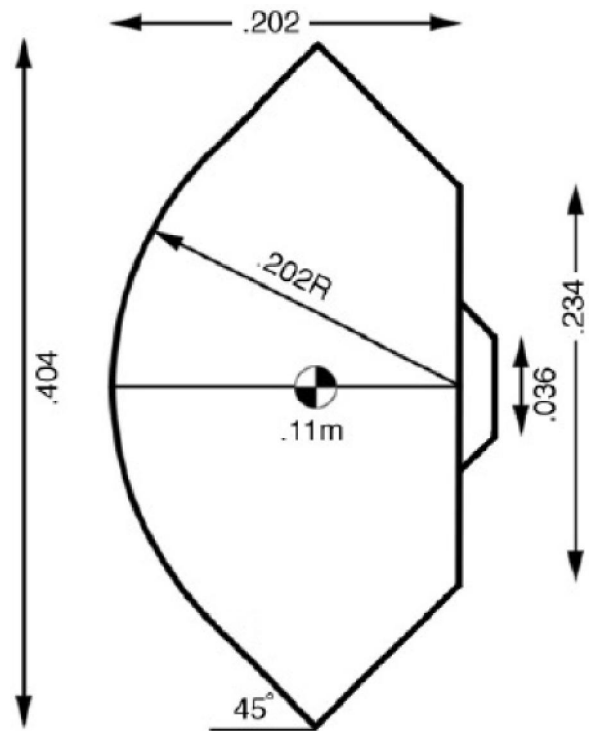


Figure 4 : HAYABUSA sample return capsule^[3].

The lower boundary of the re-entry corridor in the hypersonic phase of descent is the heat flux limit (both convective and radiative). Indeed, at high entry speeds the temperature rise in the shock layer around the capsule may be sufficiently intense for radiant heating from the hot plasma flow to be equivalent to the con-

vective heating rate. For Earth entry this occurs at speeds above 10 km/s for bluff bodies, as shown in Figure 6^[4].

In particular, Figure 6 shows radiative and convective heating rates compared for two spheres of different radii entering the Earth's atmosphere. Note that the same

equivalence in the heating processes occurs at higher speeds for objects with smaller radii, but for such capsule the temperatures in the shock would be far higher, poten-

tially compromising the temperature limits of the TPS. A possible internal and external TPS layout is shown in Figure 7.

TABLE 4 : Overview of the Hayabusa main parameters^[3].

Trajectory		Geometry		Aero/thermal		TPS	
Entry angle	-13.8°	Shape	45° sphere-cone	Trim L/D (specify trim α)	0	Material designation	Carbon-phenolic
Inertial entry velocity	11.7 km/s	Nose radius	.202 m	Ballistic coeff.	113.5 kg/m ³	Thickness	3.0 cm
Relative entry velocity	11.3 km/s	Base area	.128 m ²	Stagnation heating rate	1500 W/cm ²	Ablating? Ejected?	Yes Yes
Velocity at peak heat	10.2 km/s	Vehicle mass	16.27 kg	Integrated heat load	32,000 J/cm ²	Resin mat. Matrix mat.	
Control method	none	TPS mass fraction, inc. insul.	43%	Radiative heat flux	300 W/cm ²	Resin dens. Matrix density	
Center of Gravity, X _{CG} /D	0.28	Payload mass	1.04 kg	PH stag. pressure	0.61 atm	Total material density	1400 kg/m ³

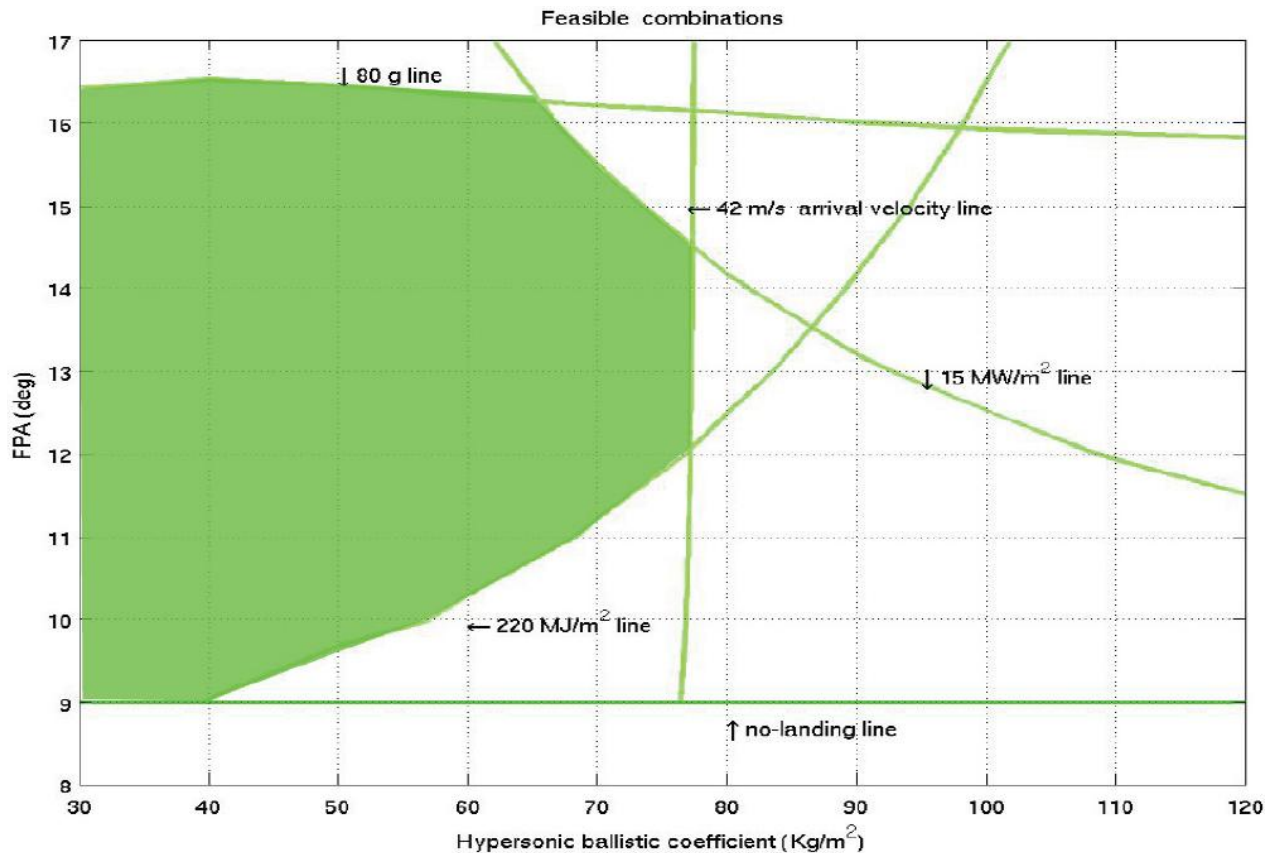


Figure 5 : Example of SRV study results: re-entry corridor^[2].

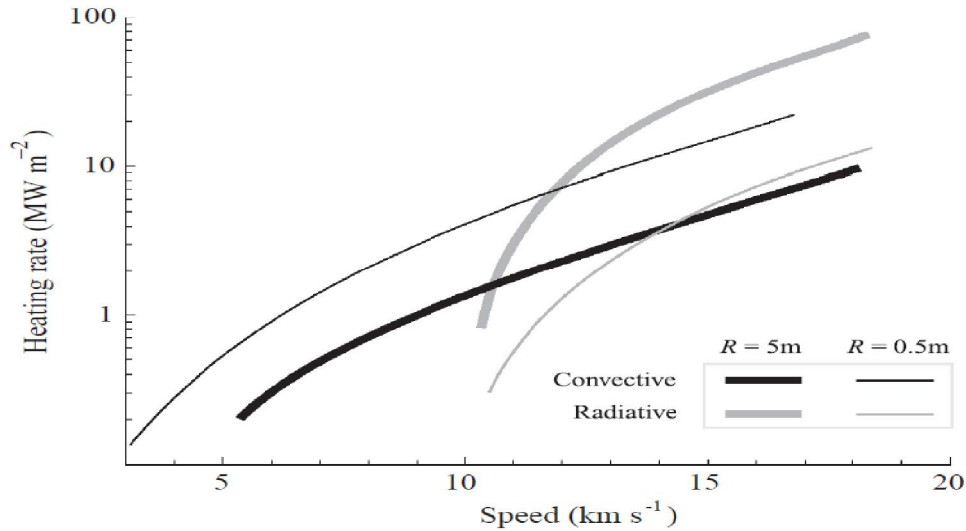


Figure 6 : Radiative and convective heating rates limits for Earth entry^[4].

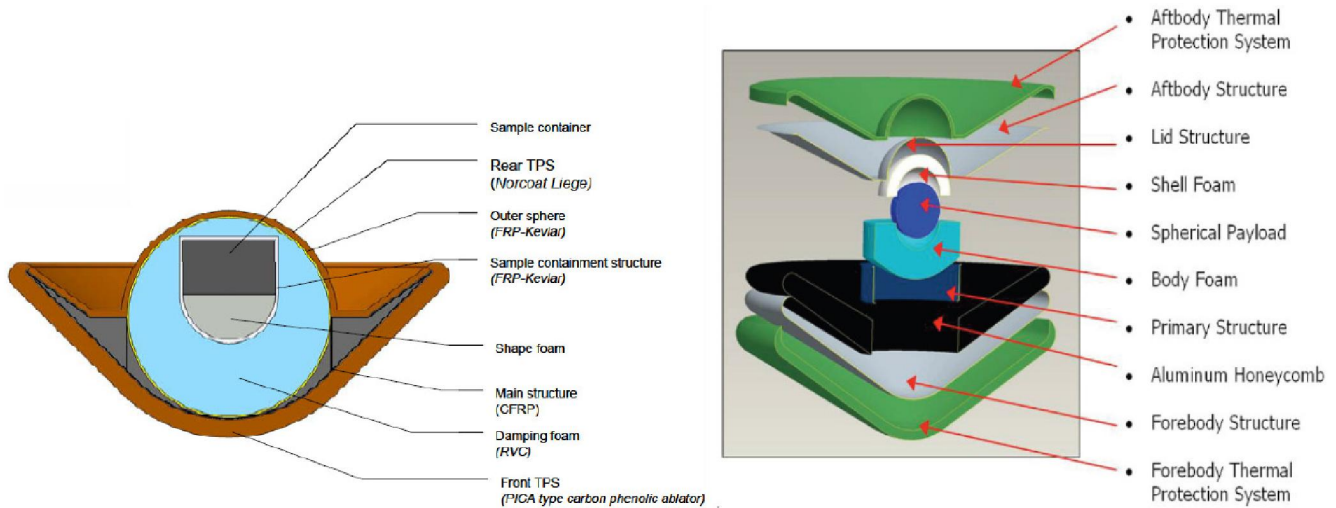


Figure 7 : Example of SRV study results: TPS layout^[2].

In this example, the TPS layout refers to PICA-like (260 kg/m³) front heatshield, Norcoat-Liege rear TPS, 45 deg half-cone angle, 1.1 m base diameter, 200 mm Reticulated Vitreous Carbon (RVC) foam, and 76 kg capsule.

Figure 8 together with Figure 9, summarized the thermal protection systems for several space missions. As we can see, there are two regression curves that can be used for the TPS preliminary design^[5].

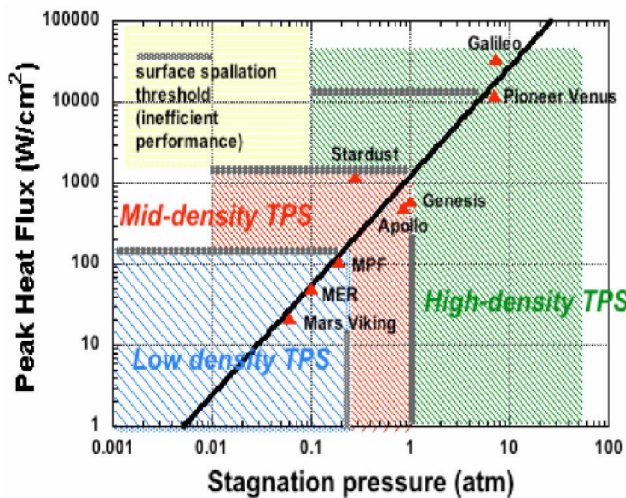


Figure 8 : Mission environments for ablative TPS applications^[5].

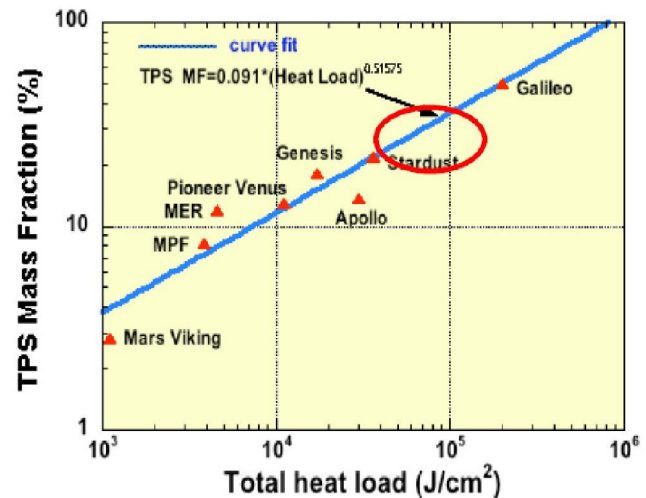


Figure 9 : TPS mass fraction for ablative heat shield missions^[5].

In fact, once stagnation pressure and peak heat flux are known, Figure 8 suggests what kind of TPS must be used; while Figure 9 gives an idea of TPS mass fraction once the total heat load is known.

Examples of SRV thermal design adopted for the Marco Polo mission is reported in Figure 10. As shown, the TPS layout of the Marco Polo SRV is made of Saffil, RVC, and CFRP (Carbon Fiber Reinforced Polymer)^[2].

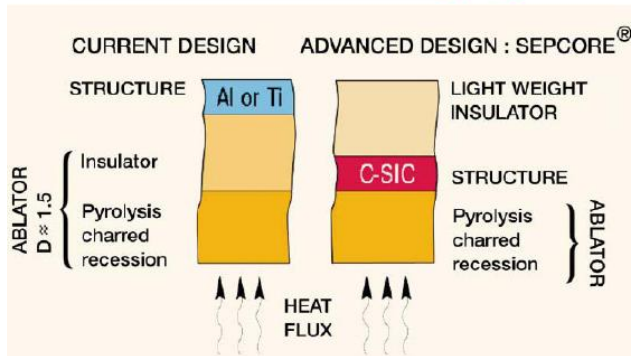
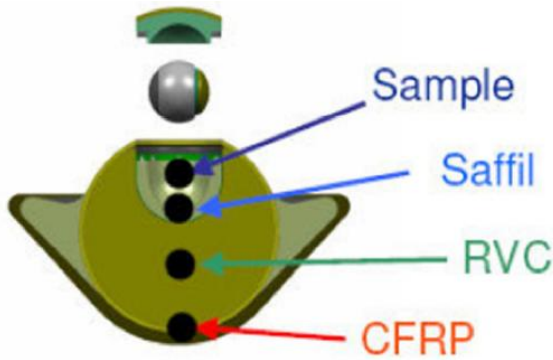


Figure 10 : Internal and external (lower side) layout of Marco Polo TPS^[2].

Some TPS materials and related properties are summarized in TABLE 5^[6].

TABLE 5 : Properties of some TPS materials^[6].

Material	Density, kg/m ³	Thermal Conductivity, ^a W/m-K	Emissivity, ^a ε	Melt Temp., K
AVCOAT 5026 (virgin)	529	0.242	0.67	1920
AVCOAT 5026 (char)	264	—	0.49	—
Carbon-Phenolic (Acusil I)	480	0.112	0.95	2000
Reinforced Carbon-Carbon (RCC)	1580	5.05 (normal) 7.88 (parallel)	0.54 to 0.9	2030 ^b
Teflon	2190	0.251	—	—
Shuttle Tile (LI-900)	144	0.047	0.88	1755 ^b
Beryllium	1840	170	—	810 ^b
Oak	610	0.146	—	—

^a Squire, 2006 (TPSX database).

^a Thermal conductivity and emissivity are functions of temperature.

^b Single-use temperature limit.

As far as capsule mass budget is concerned, in TABLE 6 are summarized examples of the impact of each capsule subsystem on the overall vehicle mass. In particular, TABLE 6 refers to Mars Sample Return Study^[2].

TABLE 6 : Examples of mass budget for SRV^[2].

Element	Mass (Kg)
Heat shield	11.19
Aftbody TPS	1.96
Primary Structure	4.71
Secondary Structures	2.96
Canisters (2)	7.20
Receptacles	1.36
Energy Absorbing Mat.	2.52
Beacons (2)	0.60
Mechanisms	1.90
Sensors and cables	0.20
Miscellaneous	1.14
Launch Total	28.53
Entry Total	35.73
Launch Total (+25%)	35.66
Entry Total (+25%)	42.86

Design analysis

Within each design loop, several sciences are involved. From Structural Mechanism, Electronics to Fluid Dynamics and etc. As a consequence, the SRV is a result of a Multidisciplinary Design Optimization (MDO)^[7].

The design process evolves through “trade-off” analysis. For example, requirements and constraints impact on design in terms of trade-off analysis that accounts for: Heat flux; Heat input; Drag; Stability; Landing accuracy; Landing conditions; Accommodation into launcher fairing; Mass; that in turns depends on mission parameters as: Entry angle; Entry velocity and etc.

Moreover, a detailed description of the flow field past the re-entry vehicle is mandatory to address the impact of several design issues^[8,9]. For instance, Computational Fluid Dynamics (CFD) analysis is necessary for the determination of convective and radiative heat fluxes, and these fluxes have a direct impact on the selection of the material for the TPS^[8]. This will allow also a more accurate determination of the TPS thickness distribution. Then, the detailed knowledge of flowfield past the re-entering vehicle allows designer to evaluate SRV aerodynamic performances as well as static and dynamic stability to improved Flight Mechanics analysis and so on^[10].

Example of design analysis, can be found in Figure 11 where is shown the flowfield predicted around the SRV at $M_\infty=22.14$). In particular, the figure shows the temperature contours reported both on the capsule pitch plane and two flowfield cross sections.

The pressure distribution over the descent module forebody is also provided. As shown, the maximum flowfield temperature is close to about 7000 K since, due

to the high Mach number, thermo-chemical processes occur behind the bow shock as species vibrational excitation and dissociation.

Moreover, three dimensional streamtraces, coloured by Mach number, past the capsule at $M_\infty=3$ and $\alpha=10$ deg and pressure distribution on the spacecraft front shielded

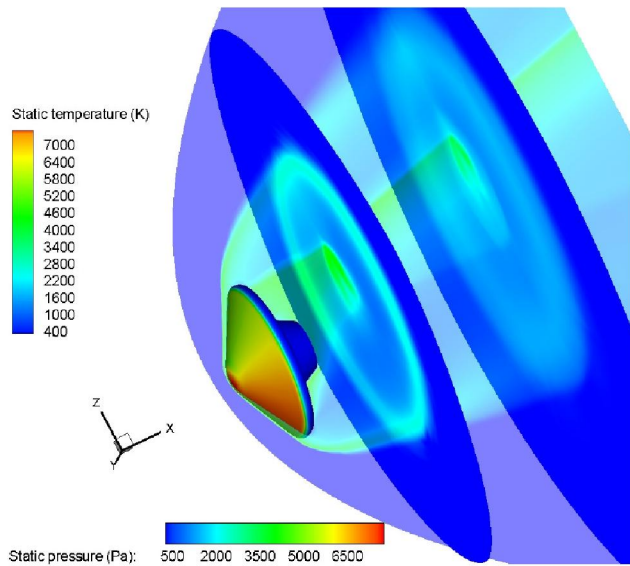


Figure 11 : The static temperature field on the capsule symmetry plane and on two flowfield cross sections at $M_\infty=22.14$ and $\alpha=10$ deg static pressure on heatshield.

can be found in Figure 12.

This figure provides very interesting flowfield features as the strong flow expansion at capsule shoulder and the complexity of the base flow.

Examples of SRV aeroheating assessment (without accounting for heat shield ablation) for flight conditions ranging from R1 to R6 trajectory points of Figure 13 are shown in Figure 14.

Figure 14 summarizes the heat flux distributions at capsule front shield centreline.

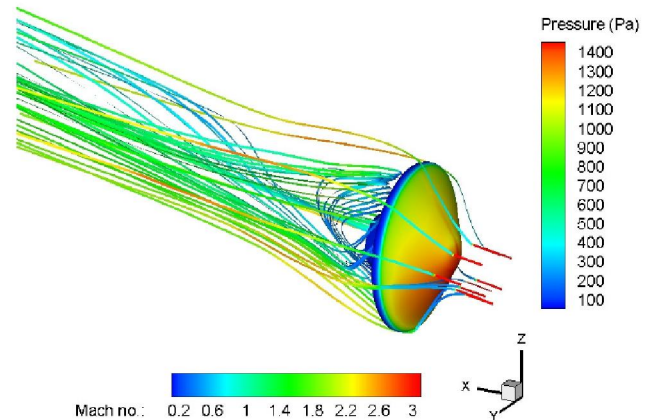


Figure 12 : Flowfield streamtraces past the capsule, coloured by Mach number and pressure distribution on heatshield at $M_\infty=3$ and $\alpha=10$ deg.

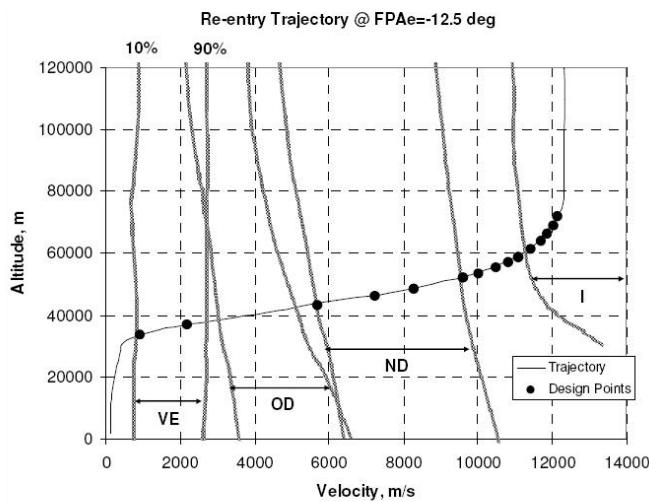


Figure 13 : Reference re-entry trajectory with CFD design points.

Results refer to convective and radiative heat fluxes at the wall. The latter one has been computed with PARADE with the density, the molar fractions and the two temperatures (translational and vibrational) of all the R trajectory points coming from CFD simulations.

As shown, Figure 14 highlights that the maximum radiative heat flux is equal to about 6 MW/m^2 and is reached

at the R3/M1 flight conditions (i.e., $H_\infty=58.73$ km altitude and $M_\infty=34.45$).

The convective peak heating reaches 8.5 MW/m^2 , and it is attained at R5/M2 trajectory point (i.e., $H_\infty=52.05$ km altitude and $M_\infty=29.12$).

Anyway, the maximum total heat flux is equal to about 12.5 MW/m^2 and it arises when the SRV is flying at

Design Points Id	Altitude [km]	Velocity [m/s]	Pressure [pa]	Density [kg/m ³]	Temperature [K]	Mach [-]
R1	71.86	12138	4.14	6.78×10^{-5}	212.41	41.54
R7	69.03	12032	6.386	9.95×10^{-5}	223.48	40.14
R8	66.25	11880	9.589	1.42×10^{-4}	234.37	38.70
R2	63.98	11711	13.19	1.88×10^{-4}	243.29	37.45
R9	61.31	11445	18.889	2.59×10^{-4}	253.19	35.87
M1/R3	58.73	11099	26.49	3.57×10^{-4}	258.26	34.45
R10	57.07	10816	32.835	4.37×10^{-4}	261.52	33.07
R4	55.46	10490	40.33	5.30×10^{-4}	264.69	32.16
R11	53.53	10022	51.459	6.67×10^{-4}	268.49	30.50
M2/R5	52.05	9604	61.84	7.95×10^{-4}	270.65	29.12
M3/R6	48.36	8280	97.84	1.25×10^{-3}	270.65	25.11
R12	46.04	7230	130.72	1.70×10^{-3}	267.03	22.07
M4	43.14	5681	189.53	2.54×10^{-3}	259.02	17.61
M5	36.93	2181	437.43	6.30×10^{-3}	241.86	7.00
M6	33.62	922	701.11	1.04×10^{-2}	232.69	3.02

$H_\infty=58.73$ km altitude and $M_\infty=34.45$ (i.e., R3/M1 TP). Therefore, plasma radiation is an additional contribution to surface aeroheating that must be taken into account in designing the SRV thermal protection system.

In particular, the generic convective heat flux profile in Figure 14 highlights that, after the peak at the stagnation point, the heat flux decreases along the heatshield surface as the boundary layer develops up to an inflection

point that corresponds at the end of the spherical shape of the capsule.

Hence, it continues to decrease along the conical part with a different shape and, then, it increases near the shoulder due to the small radius of curvature and to the expansion that causes a reduction of the boundary layer thickness.

Radiative heat flux profiles for the remaining R7 to R12 cases are quite the same as those of R1 to R6 reported in

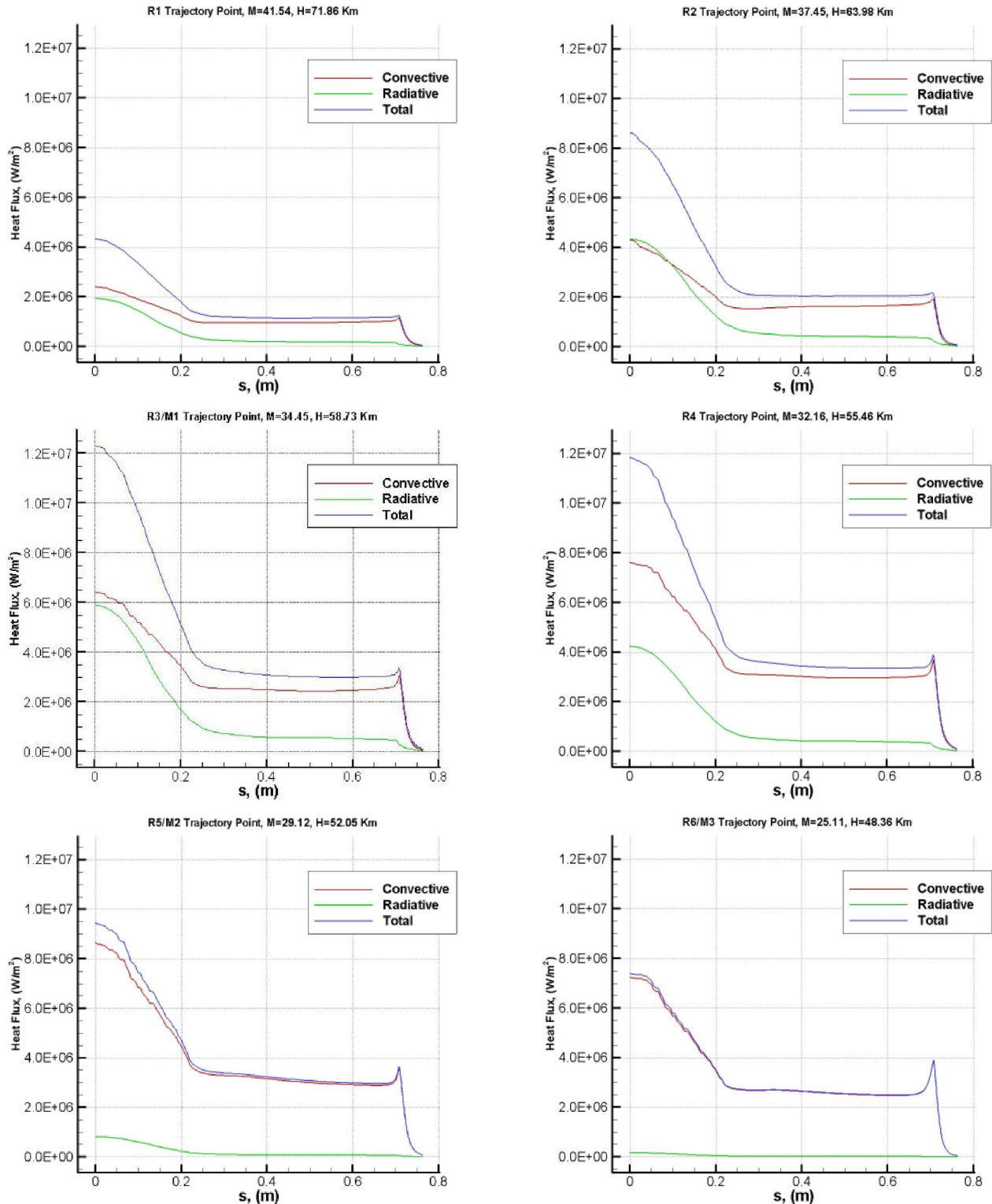


Figure 14 : Convective and radiative heat fluxes comparison for R1-R6 TPs.

Figure 14 and, therefore, are not reported for brevity. Contours field of CO species, blowing from the heat shield made of carbon-phenolic material, past a sphere-cone aeroshell (see Figure 3) flying at 55.11 km altitude and $M_\infty=31.87$ are shown in Figure 15. Note that CO is one of the main ablation products (for carbon based materi-

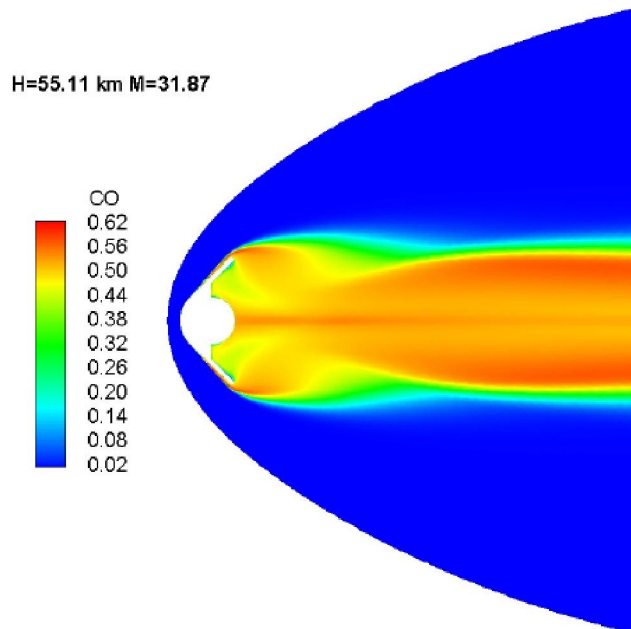


Figure 15 : CO mass fraction distribution at 55.11 km altitude and $M_\infty=31.87$.

als), and it lowers significantly the SRV wall enthalpy^[11]. Figure 15 also highlights that TPS ablation demands particular care within flowfield CFD analysis because of it may influence SRV aerothermal performance considering that: heat shield roughness promotes turbulence transition; TPS ablation determines convective and radiative aeroheating blockage because of ablation reduces the surface gradients of temperature and that of various species mass fractions, causing a decrease of convective and diffusive heat-fluxes; heatshield ablation influences the flowfield past the SRV by means of introduction of new species in the boundary layer, that in turn may increase flowfield ionization^[12].

Further example of design analysis is shown in Figure 16 where the influence of ablation on flowfield and shock stand-off distance for a high-speed Earth entry is recognized. In particular, the top figure represents non-equilibrium predictions with ablation. The bottom figure shows non-equilibrium temperature contours without taking into account for ablation^[12]. This comparison puts in evidence the influence of ablation on results of non-equilibrium simulations since the temperature predicted in the ablative case is lower than in the non-ablative one^[12]. Moreover, the shock wave is closer to the capsule in the ablative simulation. Therefore, ablation has a large influence on the non-equilibrium results and, then, has to be carefully

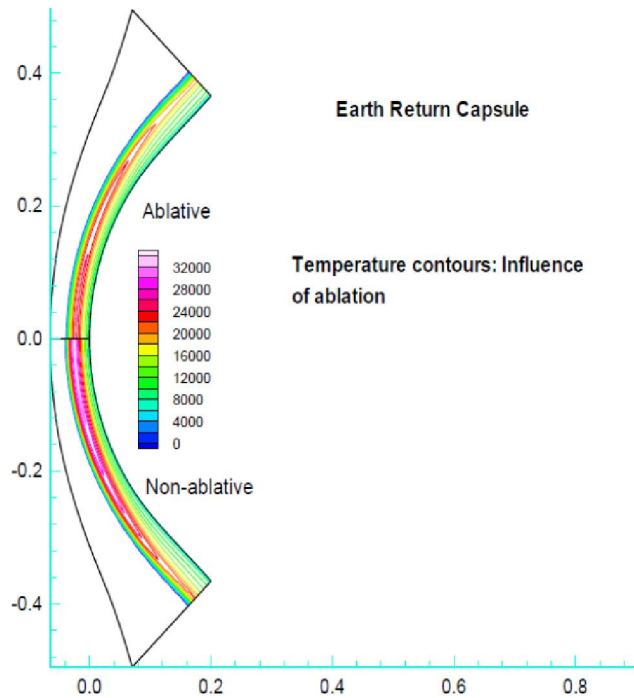


Figure 16 : Static temperature contours (K). Influence of ablation^[12].

studied to design the SRV thermal protection shield. Generally speaking, the ablation products in the boundary layer mainly consist of H_2 , C_2H , C_2H_2 , CO, C, and $H^{[11]}$. For example, the mass fraction fields of H_2 , H, CO and C that take place in the shock layer in front of a 1.1 m diameter spherically-blunted 45 deg half-angle forebody (i.e., close to that shown in Figure 7) flying at 71.86 km altitude and $M_\infty=41.54$ are reported in Figure 17 and Figure 18, respectively.

Mass fraction profiles of blowing species produced in the shock-layer by the heatshield recession are plotted along with the stagnation streamline in Figure 19.

As shown, the boundary layer in the case of species blowing is significantly different with respect to the non-ablating case^[11]. In fact, as the wall is approached the level of all of the air species fall as the presence of the blown

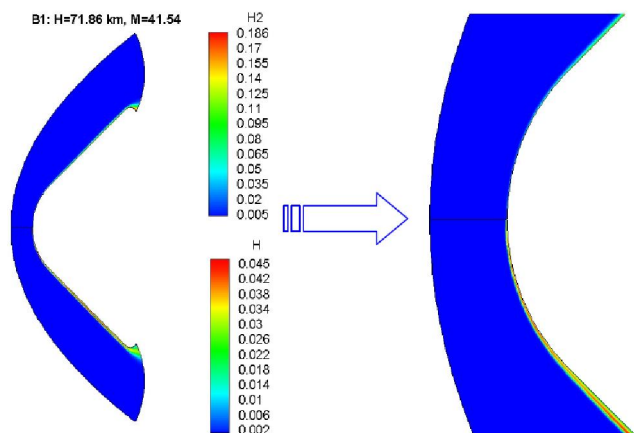


Figure 17 : H_2 and H mass fractions at $H_\infty=71.86$ km and $M_\infty=41.54$.

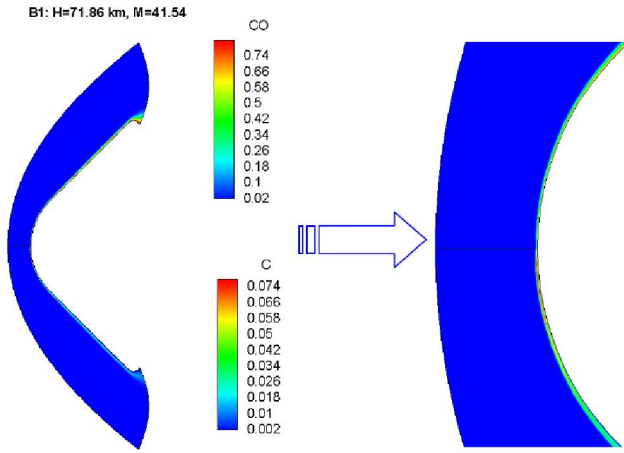


Figure 18 : CO and C mass fractions at $H_\infty=71.86$ km and $M_\infty=41.54$.

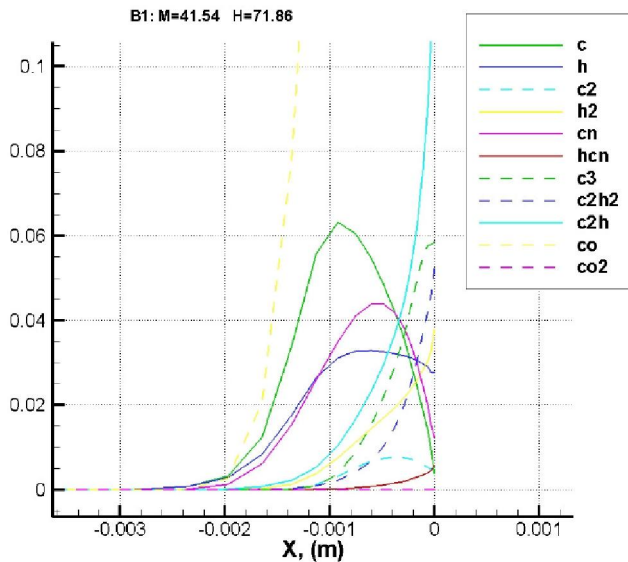


Figure 19 : Ablation products on the stagnation streamline at $H_\infty=71.86$ km and $M_\infty=41.54$.

gases becomes more dominant. Moreover, it is evident from the profiles that some of the ablation products are undergoing chemical change and it is interesting to note that although most of the ablation products are restricted to the boundary layer there is a significant level of some of these products, specifically C, at positions slightly beyond the edge of the boundary layer. As further example, flowfield features regarding freestream conditions equal to $H_\infty=57.07$ km and $M_\infty=33.07$ are recognized from Figure 20 to Figure 23. In Figure 20 static pressure and Mach number fields are shown; while Figure 21 and Figure 22 highlight C, CO, C_2 , C_3 , mass fractions, respectively. The distribution of blowing species along with the stagnation streamline is plotted in Figure 23. The knowledge of the ablation products distribution within the shock layer is extremely important since species such as C_2 , C_3 and also CO have strong radiative properties. In particular, C_2 and C_3 possess absorption properties while

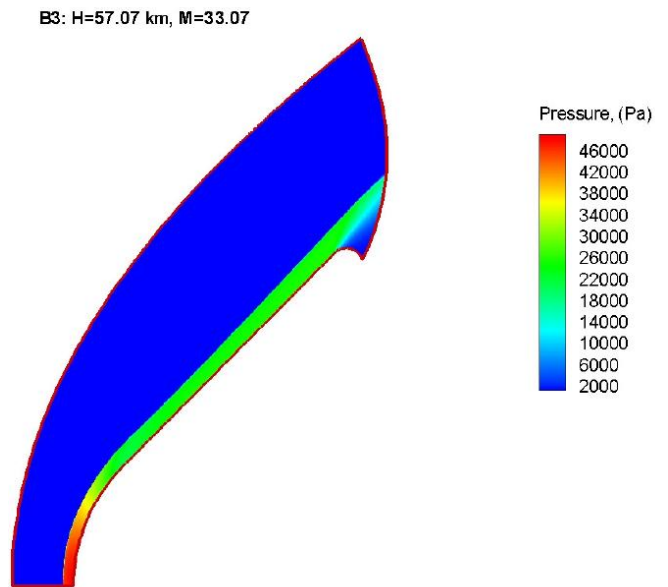
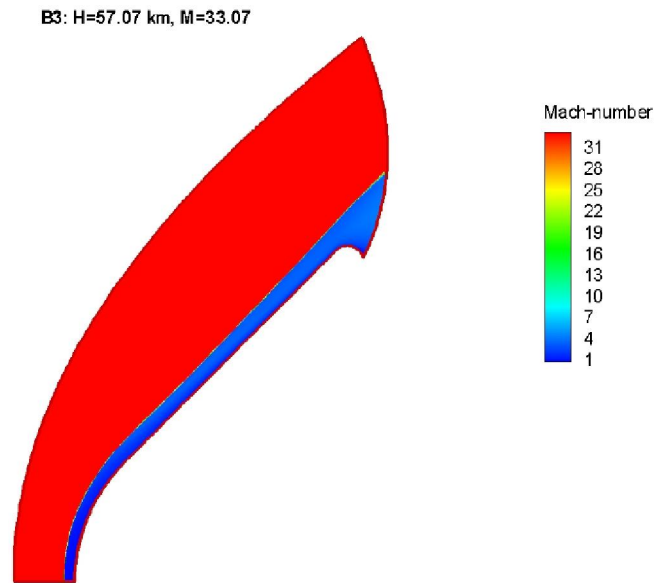


Figure 20 : Mach number and static pressure contours at $H_\infty=57.07$ km and $M_\infty=33.07$.

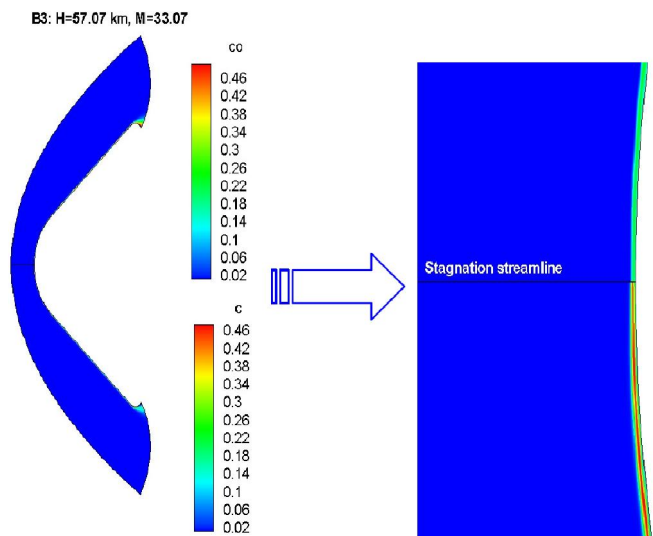


Figure 21 : CO and C mass fractions at $H_\infty=57.07$ km and $M_\infty=33.07$.

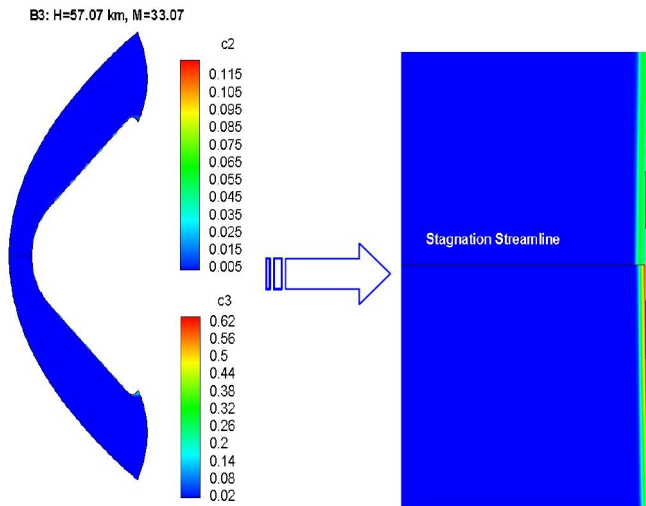


Figure 22 : C_2 and C_3 mass fractions at $H_\infty=57.07$ km and $M_\infty=33.07$.

CO is a strong radiator^[12]. As shown, the level of C_3 falls rapidly with increasing distance from the body, as it dissociates to form C_2 and C, and also indirectly leads to the formation of CN and HCN. Note that the formation of small amounts of CN induces a more severe heat flux distribution because of a major non-equilibrium radiation contribution (i.e., CN molecule is a highly emissive product). Moreover, the rise in the level of C in the boundary layer is mainly attributable to the dissociation of CO. The relatively slow rate at which the level of H falls with increasing distance from

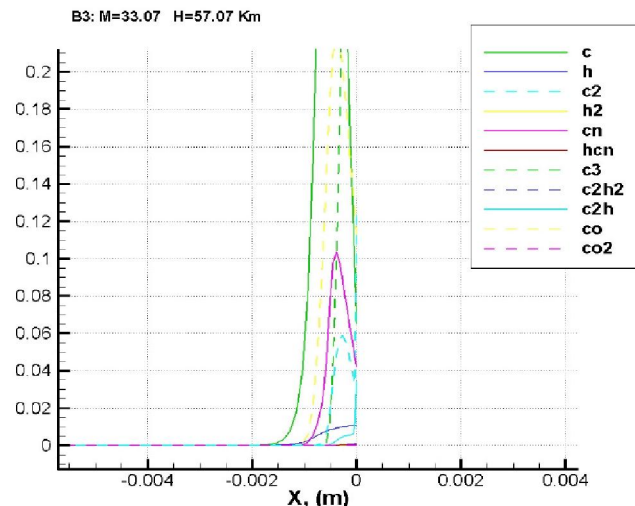


Figure 23 : Ablation products on the stagnation streamline at $H_\infty=57.07$ km and $M_\infty=33.07$.

the wall suggests that either H_2 or alternatively some of the hydrocarbons present are dissociating^[11,12]. Another important issue in designing SRV capsule is the coupling of plasma radiative effects and the CFD computation. For example, Figure 24 presents, on the left, the front shield shock layer temperature field and, on the right, temperature profiles along with the stagnation line of the Huygens probe with and without coupling effects. As shown, a reduction of the stand-off distance can be observed as well as a faster decrease of the temperature for the coupled computations due to the removal from the

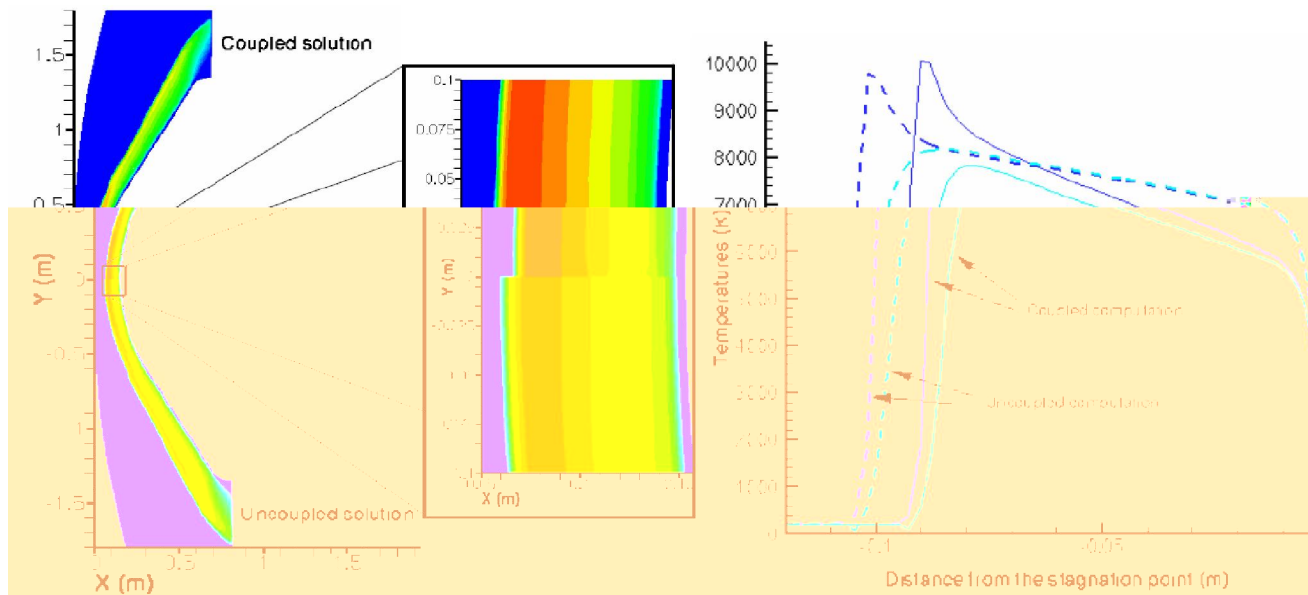


Figure 24 : Temperature contours: influence of radiation coupling within computation^[12].

flowfield by radiation phenomenon^[12].

CONCLUSION

In this paper a partial overview of the analysis approach typically followed within sample return vehicle design has

been done. A more systematic survey was out of the scope of the paper, but would be required for the preparation of ambitious sample return projects. In particular, this work gives some indications concerning main design topics to address in designing such a kind of vehicle for planetary exploration, as for example, effects of heat shield

ablation and flow plasma radiation coupling with computational flowfield analysis.

REFERENCES

- [1] Design Overview of an Asteroid Sample Return Capsule. The Institute of Space and Astronautical Science. Report SP No. 17 March (2003).
- [2] Re-entry technologies for sample return capsules; ESA/ESTEC, Aerothermodynamic Section. Alpbach, 25/7/08
- [3] Planetary Mission Entry Vehicles Quick Reference Guide; Version 3.0 NASA/SP-2006-3401
- [4] A.J., J.R.C.Garry, R.D.Lorenz, V.V.Kerzhanovich; Planetary landers and entry probes. Cambridge University Press, (2007).
- [5] B.Laub, E.Venkatapathy; Thermal protection system technology and facilities needs for demanding future planetary mission. International Workshop on Planetary Probe Atmospheric Entry and Descent Trajectory Analysis and Science, Lisbon, Portugal, 6-9 October (2003).
- [6] Notes on Earth Atmospheric Entry for Mars Sample Return Missions. NASA/TP-2006-213486, (2006).
- [7] J.Bertin; Hypersonic Aerothermodynamics. AIAA Educational Series, Washington, (1994).
- [8] Predictions of Radiative and Convective Fluxes at Stagnation Point for an Earth High-Speed Re-Entry. SP667-2009
- [9] J.Anderson; Hypersonic and High Temperature Gas Dynamics. McGraw-Hill Book Company, New York, (1989).
- [10] R.Mitcheltree; A passive Earth-Entry Capsule for Mars Sample Return. 51st International Astronautics Federation Congress, Rio de Janeiro, IAF-00-Q.3.04, (1998).
- [11] Modelling gas/Surface Interaction Processes of Ablating Wall Boundaries Associated with Planetary Entry, ESASP.367.311R, (1995).
- [12] Ph.Reynier, V.Marieu, L.Marraffa; Aerothermodynamics developments for planetary missions, Stuttgart, SAE 99, November 17-19, (1999).